

submitted to **Journal of Space Weather and Space Climate**

© The author(s) under the Creative Commons Attribution 4.0 International License (CC BY 4.0)

Energetic particle acceleration and transport with the novel Icarus+PARADISE model

E. Husidic^{1,2}, N. Wijsen¹, T. Baratashvili¹, S. Poedts^{1,3}, and R. Vainio²

¹ Centre for mathematical Plasma Astrophysics, Department of Mathematics, KU Leuven, Celestijnenlaan 200B, 3001 Leuven, Belgium
e-mail: edin.husidic@kuleuven.be

² Department of Physics and Astronomy, University of Turku, 20014 Turku, Finland

³ Institute of Physics, University of Maria Curie-Skłodowska, ul. Radziszewskiego 10, 20-031 Lublin, Poland

Received October 02, 2023; accepted March 26, 2024

ABSTRACT

With the rise of satellites and mankind's growing dependence on technology, there is an increasing awareness of space weather phenomena related to high-energy particles. Shock waves driven by coronal mass ejections (CMEs) and corotating interaction regions (CIRs) occasionally act as potent particle accelerators, generating hazardous solar energetic particles (SEPs) that pose risks to satellite electronics and astronauts. Numerical simulation tools capable of modelling and predicting large SEP events are thus highly demanded. We introduce the new Icarus+PARADISE model as an advancement of the previous EUHFORIA+PARADISE model. Icarus, based on the MPI-AMRVAC framework, is a three-dimensional magnetohydrodynamic code that models solar wind configurations from 0.1 au onwards, encompassing transient structures like CMEs or CIRs. Differing from EUHFORIA's uniform-only grid, Icarus incorporates solution adaptive mesh refinement (AMR) and grid stretching. The particle transport code PARADISE propagates energetic particles as test particles through these solar wind configurations by solving the focused transport equation in a stochastic manner. We validate our new model by reproducing EUHFORIA+PARADISE results. This is done by modelling the acceleration and transport of energetic particles in a synthetic solar wind configuration containing an embedded CIR. Subsequently, we illustrate how the simulation results vary with grid resolution by employing different levels of AMR. The resulting intensity profiles illustrate increased particle acceleration with higher levels of AMR in the shock region, better capturing the effects of the shock.

Key words. solar energetic particles – particle transport – numerical

1. Introduction

Space weather events are having an ever growing socio-economic impact on today's societies that are heavily reliant on nanotechnology, Global Navigation Satellite Systems (GNSS), and satellites

for communication (Hapgood, 2011; Schrijver et al., 2015). Solar eruptive events, especially coronal mass ejections (CMEs), stand out as the primary drivers of hazardous conditions in the inner heliosphere that spacecraft and astronauts are exposed to (Gopalswamy, 2018). Moreover, fast CMEs directed towards Earth can interact with the terrestrial magnetic field, causing geomagnetic storms and potentially affecting electrical power grids, pipelines, and telecommunication (Hapgood, 2011; Schrijver et al., 2014, 2015).

A frequent consequence of solar eruptions is the acceleration of charged particles that are collectively referred to as solar energetic particles (SEPs), comprising electrons, protons, and ions (Reames, 2017). Historically, two types of SEP events were distinguished, namely impulsive and gradual SEP events, where the first type was linked to solar flares and the second type to CMEs (Reames, 1999). However, Kallenrode (2003), and later also Cane et al. (2010), showed that the largest SEP events include contributions from both flare and CME shock acceleration. Beside solar eruptive phenomena, the shocks in corotating interaction regions (CIRs) function occasionally as particle accelerators to generate energetic particles in the inner heliosphere, and also accelerate more efficiently particles in the outer heliosphere (Richardson, 2004; Wijzen et al., 2019). A CIR is a region where a fast solar wind stream catches up a slow solar wind stream and compresses it. Some authors (Jian et al., 2006; Richardson, 2018) reserve the term CIR for interaction regions with a lifetime greater than one solar rotation, and refer to events of shorter duration as stream interaction regions (SIRs). In the present work we refer to all such interaction regions as CIRs. At radial distances well beyond 1 au, CIRs are often bounded by two shock waves, a forward shock wave accelerating the slow wind, and a reverse shock decelerating the fast wind. However, in the majority of cases observed at 1 au, CIRs are only bounded by two compression waves, and the shock waves form further out (Richardson, 2018). In observational data, the suprathermal particle intensity profiles often show a double-peaked profile as a result of particles being accelerated at both the forward and reverse shock/compression waves (Smith and Wolfe, 1976; Richardson, 2018; Allen et al., 2021; Wijzen et al., 2021).

In large SEP events, accelerated particles can achieve energies of several hundreds of MeV/nuc or even up to a few GeV/nuc, posing a dangerous threat to satellites and astronauts. Therefore, there is significant interest in understanding the acceleration and transport processes behind SEP events. Despite huge and decades-long efforts, there is still no consensus in the scientific community about the exact acceleration mechanisms for SEPs (Petrosian, 2016; Perri et al., 2022). A frequently proposed candidate for the acceleration mechanism in impulsive events at solar flare sites during magnetic reconnection is stochastic acceleration (SA) due to turbulence (Petrosian and Liu, 2004). Possible explanations for the acceleration of SEPs at shock fronts include diffusive shock acceleration (DSA) and shock drift acceleration (SDA), accompanied by SA (Desai and Giacalone, 2016; Vainio and Afanasiev, 2018). In the SDA mechanism that occurs when the charged particle interacts with a quasi-perpendicular shock front, the particle travels multiple times upstream and downstream the shock. The difference in magnetic field strengths in the two regions leads to a change in the cyclotron radius of the particle which shift the particle's guiding centre along the electric field, resulting in a continuous acceleration. The DSA mechanism dominates at quasi-parallel shocks. Here, the charged particle also crosses multiple times the shock front to gain energy, but is scattered at frozen-in magnetic turbulence on both sides of the shock, altering the particle's pitch angle. The SA occurs due to resonant wave-particle interactions between the SEP and magnetic field

fluctuations (for more details on the acceleration mechanisms, see e.g., [Kallenrode 2004](#); [Vainio and Afanasiev 2018](#)).

In recent years, several simulation models have been developed both for theoretical studies and the forecasting of SEP and CIR events, characterised by a common feature, the coupling of a heliospheric solar wind model with a particle transport code. A few of these models shall be mentioned in the following. The SEP_{MOD} (Solar Energetic Particle _{MODEL}) developed by [Luhmann et al. \(2017\)](#) uses background solar wind configurations generated by the heliospheric three-dimensional (3D) magnetohydrodynamic (MHD) model Enlil ([Odstreil et al., 2004, 2005](#)) to simulate the scatter-free transport of SEPs. Another SEP propagation model is the Energetic Particle Radiation Environment Module (EPREM), which includes diffusion and drift effects of the particles, introduced by [Kozarev et al. \(2010\)](#). EPREM was initially coupled to the ENLIL model ([Kozarev et al., 2010](#)), while later [Kozarev et al. \(2013\)](#) advanced EPREM to take input from the Block Adaptive Tree Solar-Wind Roe Upwind Scheme (BATS-R-US) model ([Manchester IV et al., 2012](#)). Recently, the PArTicle Radiation Asset Directed at Interplanetary Space Exploration (PARADISE) code ([Wijsen, 2020](#)) has been introduced that uses solar wind background configurations by the heliospheric 3D MHD model EUropean Heliospheric FORecasting Information Asset (EUHF_{FORIA}; [Pomoell and Poedts 2018](#)) to propagate SEPs as test particles and calculate the intensity distributions of the energetic particles. Similar to ENLIL, EUHF_{FORIA} incorporates a uniform equidistant grid. EUHF_{FORIA}+PARADISE has been applied successfully both in theoretical studies with synthetic solar wind maps ([Wijsen et al., 2019](#)) and by reproducing real SEP events ([Wijsen et al., 2021, 2023](#)).

In the present work, we introduce our new model, Icarus+PARADISE. Similar to EUHF_{FORIA}, Icarus is a 3D MHD heliospheric wind model that simulates solar wind configurations from 0.1 au onward, and models the propagation and evolution of transient structures such as CMEs and CIRs ([Verbeke et al., 2022](#)). When Icarus uses an equidistant grid, it functions similarly to EUHF_{FORIA} or ENLIL. However, unlike the latter models, Icarus can incorporate advanced numerical techniques such as radial grid stretching and (solution) adaptive mesh refinement (AMR), to increase or lower the spatial resolution in selected regions of the computational domain. For demonstration purposes, we choose in this work a synthetic idealised solar wind map to provide the inner boundary conditions at 0.1 au. In the resulting heliospheric solar wind model that contains CIRs, we use our particle transport code PARADISE to inject 1 MeV protons in the forward and reverse shock of the CIR. By solving the focused transport equation (FTE; see e.g., [van den Berg et al. 2020](#) and references therein), intensities of the energetic particles are obtained. To validate our new model, we compare simulation results to the EUHF_{FORIA}+PARADISE model that has been successfully tested with real data. Finally, we apply different levels of AMR to the background solar wind configurations of Icarus and show the significance of an increased resolution at the shock waves for the obtained particle intensities.

The paper is structured as follows. In Sec. 2 we describe the energetic particle code PARADISE (Sec. 2.1), the heliospheric models Icarus and EUHF_{FORIA} (Sec. 2.2), the setup for the subsequent simulations (Sec. 2.3) as well as considerations made for the coupling of PARADISE to Icarus (Sec. 2.4). Results of the simulations are displayed in Sec. 3, where the Icarus+PARADISE model is validated by reproducing results of the established EUHF_{FORIA}+PARADISE model (Sec. 3.1), and subsequently applied with different levels of AMR (Sec. 3.2). The paper concludes with a summary and discussion in Sec. 4.

2. Numerical models and setup

The Icarus+PARADISE model represents a coupling of two models. The PARADISE code is used to calculate the spatio-temporal evolution of energetic particles, and its functionality and setup are described in Sec. 2.1. PARADISE requires as input background solar wind configurations which are provided by the Icarus code. Together with the previously coupled EUHFORIA model that is used here to validate the Icarus+PARADISE, the two heliospheric models are illustrated in Sec. 2.2. The setup for the simulations in Sec. 3 is described in Sec. 2.3, while Sec. 2.4 outlines considerations and challenges regarding the coupling of PARADISE to Icarus.

2.1. The PARADISE code

PARADISE is a particle transport code utilised for solving the focused transport equation (FTE) to derive spatio-temporal distributions of energetic particles (Wijsen, 2020). The FTE (Roelof, 1969; Skilling, 1971, 1975; Ruffolo, 1995; Isenberg, 1997; le Roux and Webb, 2009) can be derived from the Vlasov equation under the assumption that the energetic particles propagate as test particles through a prescribed solar wind background. It describes the evolution of the five-dimensional gyrotropic particle distribution function $f(\mathbf{x}, p, \mu, t)$, which depends on various parameters: spatial coordinates \mathbf{x} , momentum magnitude p , pitch angle cosine $\mu \equiv \cos(\alpha)$ with pitch angle $\alpha = \arctan(v_{\perp}/v_{\parallel})$ where, respectively, v_{\perp} and v_{\parallel} denote the velocity components perpendicular and parallel with respect to the ambient mean magnetic field, and time t . PARADISE implements the FTE in the form

$$\frac{\partial f}{\partial t} + \frac{d\mathbf{x}}{dt} \cdot \nabla f + \frac{d\mu}{dt} \frac{\partial f}{\partial \mu} + \frac{dp}{dt} \frac{\partial f}{\partial p} = \frac{\partial}{\partial \mu} \left(D_{\mu\mu} \frac{\partial f}{\partial \mu} \right) + \nabla \cdot (\boldsymbol{\kappa}_{\perp} \cdot \nabla f) \quad (1)$$

with $D_{\mu\mu}$ being the pitch angle diffusion coefficient, $\boldsymbol{\kappa}_{\perp}$ the spatial cross-field diffusion tensor (see below for details). The total derivatives of \mathbf{x} , μ , and p in Eq. (1) are given by

$$\frac{d\mathbf{x}}{dt} = \mathbf{V}_{\text{sw}} + \mathbf{V}_d + \mu v \mathbf{b}, \quad (2)$$

$$\frac{d\mu}{dt} = \frac{1 - \mu^2}{2} \left(v \nabla \cdot \mathbf{b} + \mu \nabla \cdot \mathbf{V}_{\text{sw}} - 3 \mu \mathbf{b} \mathbf{b} : \nabla \mathbf{V}_{\text{sw}} - \frac{2}{v} \mathbf{b} \cdot \frac{d\mathbf{V}_{\text{sw}}}{dt} \right), \quad (3)$$

$$\frac{dp}{dt} = \left[\frac{1 - 3\mu^2}{2} (\mathbf{b} \mathbf{b} : \nabla \mathbf{V}_{\text{sw}}) - \frac{1 - \mu^2}{2} \nabla \cdot \mathbf{V}_{\text{sw}} - \frac{\mu}{v} \mathbf{b} \cdot \frac{d\mathbf{V}_{\text{sw}}}{dt} \right] p. \quad (4)$$

Here, \mathbf{V}_{sw} denotes the solar wind bulk velocity, \mathbf{V}_d the drift velocity of a particle's guiding center (GC) accounting for magnetic drifts (in the present work we are not concerned with GC drifts and thus set $\mathbf{V}_d = \mathbf{0}$), $v \equiv p/(\gamma m)$ is the particle speed with γ being the Lorentz factor and m the particle rest mass, and \mathbf{b} the unit vector in direction of the mean magnetic field. Furthermore, the colon in Eqs. (3) and (4) denotes the Frobenius inner product, which can be expressed by using Einstein's summation convention as $\mathbf{b} \mathbf{b} : \nabla \mathbf{V}_{\text{sw}} = b_{ij} \partial v_i / \partial x_j$. The FTE in Eqs. (1) to (4) is written in mixed coordinates, that is, the spatial coordinates are measured in an observer's inertial frame, while the momentum magnitude and the pitch angle are given in a frame co-moving with the solar wind. We note that Eqs. (1) – (4) ignore terms of the order of V_{sw}/c , where c denotes the speed of light. This is a reasonable approximation, given that $V_{\text{sw}}/c \sim 10^{-3}$. For a derivation of the FTE

retaining terms of higher order in V_{sw}/c , see for instance, Ch. 2 of [Wijsen \(2020\)](#), and references therein. Inside PARADISE, Eqs. (1) to (4) are rewritten to an equivalent set of stochastic differential equations (SDEs) that are integrated forward in time using Itô calculus ([Wijsen, 2020](#); [Strauss and Effenberger, 2017](#)).

Global heliospheric MHD models, such as EUHFORIA and Icarus (see Sec. 2.2), derive large-scale solar wind configurations, where the interplanetary magnetic field (IMF) follows a nominal spiral pattern unless it is perturbed by transient structures like CMEs and CIRs. However, even in the absence of such structures, on small spatial and temporal scales, the IMF exhibits turbulent fluctuations that are not captured by the MHD model and which can, for instance, scatter the energetic particles. In the FTE, the effect of such turbulent fluctuations on the energetic particle transport is modelled through a set of diffusion processes in phase space. An expression of these diffusion coefficients can be derived from, for instance, quasi-linear theory ([Jokipii, 1966](#)).

In PARADISE, the diffusion processes are treated in a modular fashion, that is, the diffusion terms in the FTE describing turbulence can be added, removed, or exchanged. PARADISE contains different expressions for the pitch angle diffusion coefficient which are derived under the assumption of quasi-linear theory (QLT) and magnetic slab turbulence (see e.g., [Jokipii 1966](#) or [Jackel and Schlickeiser 1992](#)). In the present work, we use an expression similar to those of [Agueda et al. \(2008\)](#) and [Agueda and Vainio \(2013\)](#), given by

$$D_{\mu\mu} = D_0 \left(\frac{|\mu|}{1 + |\mu|} + \epsilon \right) (1 - \mu^2). \quad (5)$$

Here, ϵ describes a parameter to resolve the resonance gap at $\mu = 0$ (see e.g., [Klimas and Sandri 1971](#); in the present work, $\epsilon = 0.048$), and the scaling factor D_0 is determined by the particle's rigidity and assuming a parallel mean free path (MFP) that is constant in space. In particular, we take the parallel MFP as $\lambda_{\parallel} = 0.3$ au for a 1 MeV proton. For details, we refer to [Wijsen \(2020\)](#).

Beside pitch angle diffusion, we consider also cross-field spatial diffusion (CFD) described by the diffusion tensor κ_{\perp} . Spatial CFD is a proposed mechanism to explain, for instance, SEP events that are observed by spacecraft which are seemingly not magnetically connected to the particle source (e.g., [Klassen et al., 2015](#)). In this work, we account for CFD in the PARADISE simulations by prescribing a constant perpendicular MFP length of $\lambda_{\perp} = 3 \times 10^{-4}$ au. Thus, with $\lambda_{\perp}/\lambda_{\parallel} = 10^{-3}$, the particles will predominantly propagate along the IMF lines in our simulations.

2.2. Heliospheric solar wind models

Icarus, as detailed in [Verbeke et al. \(2022\)](#) and [Baratashvili et al. \(2022\)](#), operates within a reference frame corotating with the Sun. Icarus solves the ideal 3D MHD equations to obtain heliospheric solar wind configurations from 0.1 au onward. A simple Icarus solar wind and a cone CME model is maintained as a test case in the Message Passing Interface - Adaptive Mesh Refinement Versatile Advection Code (MPI-AMRVAC), which constitutes a collection of various numerical schemes tailored for handling (near-)conservation laws and shock problems in hydrodynamics and magnetohydrodynamics ([Keppens et al., 2012](#); [Xia et al., 2018](#)). One notable feature of Icarus is its flexibility regarding the choice of a coronal model that provides the inner boundary conditions, as long as the solar wind is considered super-Alfvénic at 0.1 au (in fact, the speed has to be above the fast magnetosonic speed). While this is a common approach in MHD solar wind modelling, recent

observations by the Parker Solar Probe indicate that the solar wind can still be sub-Alfvénic at distances beyond 0.1 au (Bandyopadhyay et al., 2022; Jiao et al., 2024). Moreover, Icarus is able to exploit the output of EUHFORIA’s coronal model (see next paragraph), providing it with the inner boundary conditions. The time advantage of radial grid stretching and AMR applications in Icarus compared to simulations of EUHFORIA employing an equidistant grid has been demonstrated in studies conducted by Verbeke et al. (2022) and Baratashvili et al. (2022).

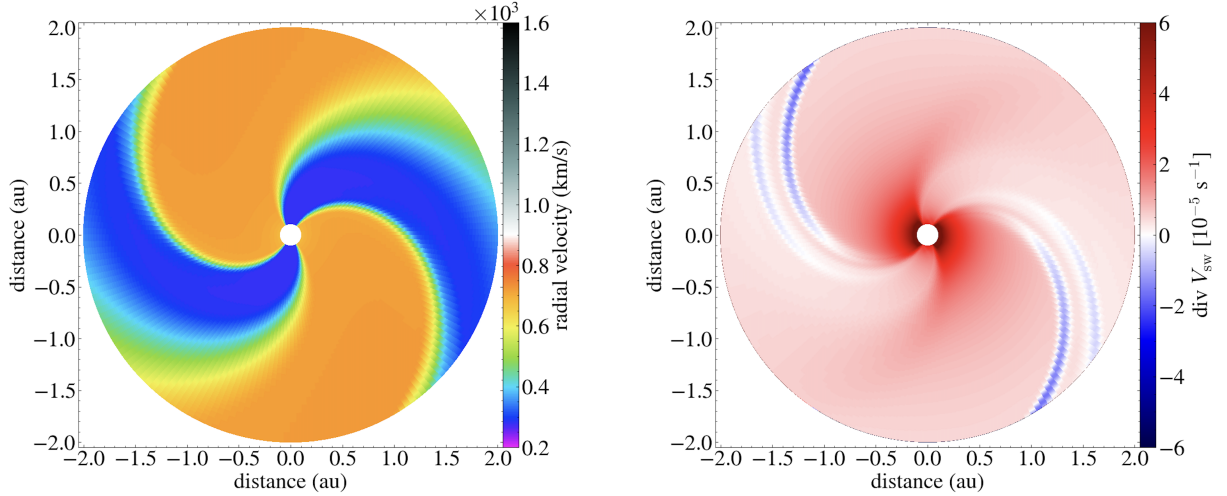


Fig. 1: Contour plots showing the radial velocity component in the ecliptic plane from 0.1 au to 2 au by Icarus (left panel), and the corresponding divergence of the solar wind velocity in the Icarus simulation.

EUHFORIA is a physics-based space weather forecasting tool that generates solar wind configurations similar to Icarus from 0.1 au onward, including transient structures such as CMEs (Pomoell and Poedts, 2018). The model comprises two primary components, a coronal and a heliospheric part. The semi-empirical coronal model accepts as input synoptic magnetograms by the Global Oscillation Network Group (GONG) and employs the Wang-Sheeley-Argue model in order to obtain the solar wind parameters at the inner boundary. Using these solar wind parameters as inner boundary conditions, the heliospheric part of EUHFORIA solves the ideal 3D MHD equations to generate solar wind configurations from 0.1 au onwards. Unlike Icarus, EUHFORIA solves the ideal MHD equations using Heliocentric Earth EQUatorial (HEEQ) coordinates with Earth’s longitude fixed at 0° on an equidistant grid without the ability of AMR.

2.3. Simulation setup

For the simulations outlined in Sec. 3 we use the following setup. The background solar wind of Icarus is displayed in the left panel of Fig. 1 and was obtained by using a synthetic solar wind map at the inlet boundary, 0.1 au, for the heliospheric wind model. The map is displayed in Fig. 2 and shows the radial solar wind velocity component of a tilted slow solar wind stream embedded in a fast wind stream which is based on the work in Pizzo (1991). The band of slow solar wind represents a wind coming from a helmet streamer around the magnetic equator of the Sun. Such a

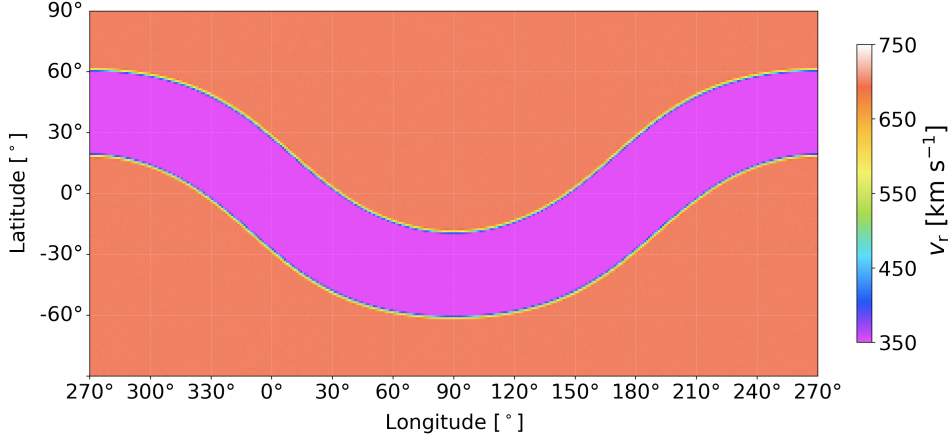


Fig. 2: Contour plot of the radial speed at the inner boundary both for Icarus and EUHFORIA.

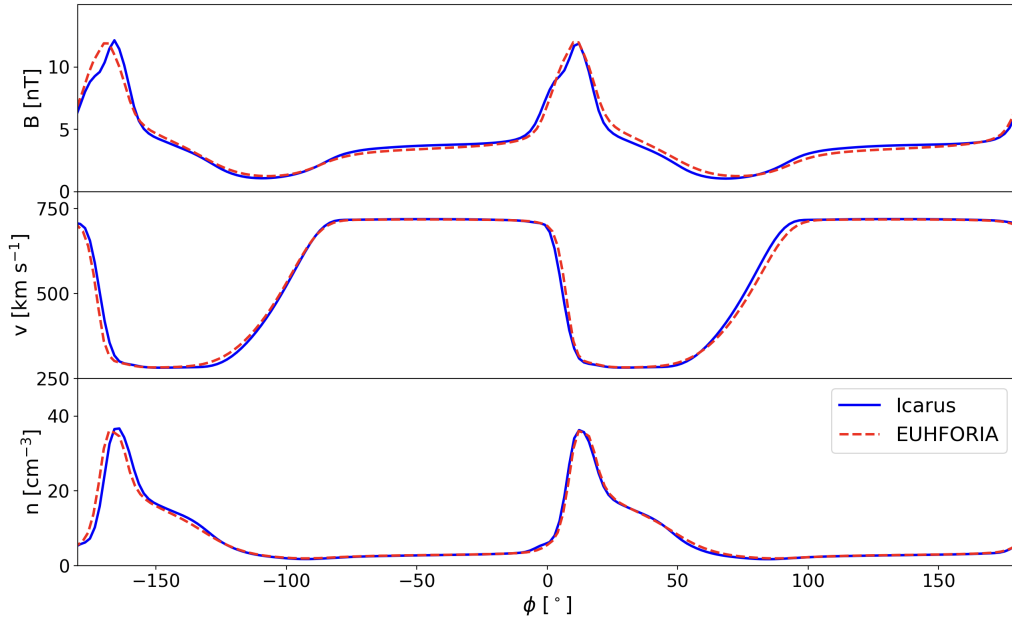


Fig. 3: Plots of the magnetic field magnitude (top panel), the solar wind speed (middle panel), and the solar wind particle number density (bottom panel) versus longitude ϕ at radial distance $r = 1$ au and colatitude $\theta = 90^\circ$ obtained by Icarus (blue solid line) and EUHFORIA (red dashed line).

configuration produces two CIRs as shown in Fig. 1. Following Pizzo (1991), in all simulations it is assumed that the magnetic axis of the Sun is tilted by 30° with respect to its rotation axis.

To determine the injection region for the test particles, we compute the divergence of the solar wind velocity of the heliospheric wind. As an example, in the right panel of Fig. 1, we present a cross-section at $\theta = 90^\circ$ of the solar wind velocity divergence in the Icarus wind. The forward and reverse shocks of the CIR are clearly identifiable where the velocity divergence is negative. Given the perfect symmetry of this structure, we arbitrarily select the the CIR that extends to the lower half-plane of the right panel of Fig. 1 for injecting 1 MeV protons within a region spanning from

0.12 to 2 au, and limited in colatitude in the interval $90^\circ \pm 2^\circ$ at the shock wave. We note that an injection energy on the order of 1 MeV is significantly higher than the anticipated energies of seed particle populations at CIR shocks. This divergence arises from the primary objective of our present study, which is to validate our model and illustrate the impact of AMR on acceleration efficiency within the model, rather than replicating a real CIR event.

The particles are injected according to the differential intensity formula, represented as

$$j(r, E) = C \delta(E - 1 \text{ MeV}) r^{-2} \quad (6)$$

with C being a proportionality constant and δ the Dirac delta distribution, and where $\text{div } \mathbf{V}_{\text{SW}} < 0$ and $j = p^2 f$. In practical terms, this is accomplished within PARADISE by uniformly distributing 1 MeV protons throughout the region where $\text{div } \mathbf{V}_{\text{SW}} < 0$ (tracing the CIR shock) and assigning them a statistical weight of $1/r^2$. To trace the shock, we used a modified version of the shock tracer code by [Wijzen et al. \(2022\)](#). Furthermore, we assume that j is independent of time. To achieve this, we first calculate the Green's function solution for the FTE, which emerges when all particles are injected at time $t = 0$. Subsequently, we derive the steady-state solution for particle injection with constant time dependence by convolving the Green's function solution with a time-independent function. This is done for all simulations in Sec. 3.

For the application of AMR in Sec. 3.2, we use a region criterion to determine the refinement location, constraining the injection region to one CIR. Following the approach outlined in [Wijzen et al. \(2021\)](#) and [Verbeke et al. \(2022\)](#), we estimate the longitudinal position $\hat{\phi}$ of the CIR that we wish to refine by

$$\hat{\phi} = \phi + \frac{r - r_B}{U} \Omega. \quad (7)$$

In Eq. (7), $[r, \phi]$ denote coordinates in the domain, r_B is the radial distance at the inner boundary (i.e., 0.1 au), U is the characteristic speed of the fast stream (in the present work, $U = 500 \text{ km s}^{-1}$), and Ω is the solar synodic rotation rate ($\Omega \approx 2.67 \cdot 10^{-6} \text{ s}^{-1}$). To approximate the CIR spiral, Eq. (7) must satisfy the condition

$$\phi_{\text{lower}} < \hat{\phi} < \phi_{\text{upper}}, \quad (8)$$

with ϕ_{lower} and ϕ_{upper} denoting the upper and lower longitudinal limits, respectively. We note that the standard setting of Icarus uses the solar sidereal rotation rate, but since EUHFORIA uses the solar synodic rotation rate, we adjusted it for the present study.

The MPI-AMRVAC framework contains a number of numerical schemes and shock capturing methods that can be selected. In this particular study, we choose the second-order (in time and space) total variation diminishing Lax-Friedrichs (TVDLF) scheme as our shock-capturing method ([Tóth and Odstreil, 1996](#)) combined with the Woodward limiter ([Woodward and Colella, 1984](#)). The TVDLF is a robust scheme, but more diffusive in comparison to other solvers, such as the Harten-Lax-van Leer (HLL) Riemann solver. A key distinction between EUHFORIA and Icarus is that in EUHFORIA $\nabla \cdot \mathbf{B}$ is prescribed to be 0. While MPI-AMRVAC has the option to also use a constraint transport approach, in Icarus, small non-zero values of $\nabla \cdot \mathbf{B}$ are locally allowed. The parabolic cleaning method by [Keppens et al. \(2003\)](#) is included, which diffuses any local non-zero divergence of the magnetic field.

To validate the Icarus+PARADISE model in Sec. 3.1, we conducted simulations replicating outcomes of the EUHFORIA+PARADISE model. To achieve this, we generated a similar heliospheric wind in EUHFORIA, employing the same coronal map utilised for Icarus, as presented in Fig. 2. In Fig. 3, we provide a comparison of the longitudinal profiles of the magnetic field magnitude (top panel), the solar wind speed (middle panel), and the particle number density (bottom panel) at 1.0 au and $\theta = 90^\circ$. The results are in reasonable agreement with slight differences in all three solar wind parameters which are due to the entirely different numerical schemes used in EUHFORIA and Icarus. The spatial domain of both winds covers a radial distance of 0.1 au to 2 au, since particle acceleration in CIRs often occurs beyond 1.0 au, and a colatitudinal and longitudinal range of 30° to 150° and 0° to 360° , respectively. The resolution of both winds is the same with 600 cells in radial direction or $\Delta r \approx 1.2 R_S$, 60 cells in colatitude and 180 cells in longitude, which corresponds to an angular resolution of $\Delta\theta = \Delta\phi = 2^\circ$.

The simulations for the comparison of different levels of AMR in Sec. 3.2 utilise the same Icarus solar wind as in Sec. 3.1. However, on AMR level 1, which corresponds to a uniform initial grid, we choose a low resolution of only 300 cells in radial direction, 40 cells in colatitude and 96 cells in longitude. With each subsequent AMR level, the number of cells in each direction doubles, at least locally, i.e., where the given AMR criteria are satisfied. In the highest AMR level achievable in the chosen simulation setup, AMR level 5, there are 'effectively' 4800 cells in the radial direction, 640 'effective' cells in colatitude, and 1536 'effective' cells in longitude, reflecting the highest refinement level.

Finally, we note that we made two modifications in the inner boundary conditions in comparison to the standard Icarus version available in MPI-AMRVAC. Since larger discrepancies in v_ϕ and B_ϕ in Icarus and EUHFORIA at and near the inner boundary were noticed resulting from the use of different coordinate systems, we changed the inner boundary in Icarus to match those in EUHFORIA. The longitudinal velocity component at the inner boundary was altered to $v_\phi = -r_B \Omega \sin(\theta)$ in order to obtain $v_\phi \approx 0$ at the inner boundary in the inertial frame. According to [Pomoell and Poedts \(2018\)](#), we also adjusted the longitudinal magnetic field component to $B_\phi = B_r v_\phi / v_r$, where B_r and v_r are the radial magnetic and velocity component, respectively. This change in B_ϕ was made to ensure that the electric field is zero in the corotating frame, a necessary condition for obtaining a steady-state solution of the solar wind in the corotating frame, as implemented in EUHFORIA.

2.4. Coupling of PARADISE to Icarus

The PARADISE particle transport code employs a grid-free numerical approach for the propagation of energetic test particles. However, the input background solar wind configurations required by PARADISE are provided on a numerical grid, containing parameters of the solar wind plasma. To integrate the set of equations constituting the FTE for a specific particle, it becomes necessary to locate the test particle on the numerical grid of the particular heliospheric solar wind model, read out the solar wind plasma variables of the grid points surrounding the particle, and interpolate them at each computational step. For this purpose, the method of trilinear interpolation that has been applied for the previously coupled EUHFORIA model has been adopted also for the implementation of the Icarus model due to the rectangular arrangement of solar wind variables within Icarus.

While EUHFORIA utilises a uniform and equidistant grid contained in a single large rectangular block, the Icarus grid adopts a more complex structure comprising multiple blocks. In the case of

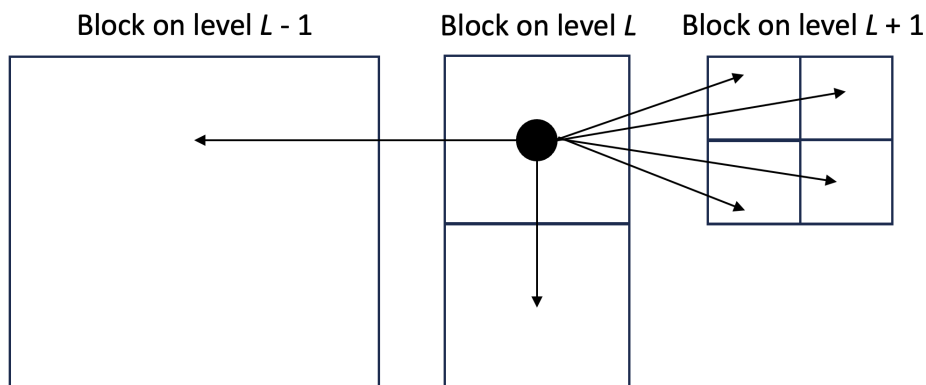


Fig. 4: Illustration of the AMR nesting and communication between blocks. Using AMR likely requires blocks of some level L to communicate both to coarse blocks (level $L - 1$) and further refined blocks (level $L + 1$).

Icarus, each level of refinement divides the target block into halves along each coordinate direction. As higher levels of AMR are applied, these blocks with different AMR levels follow a strict nesting protocol, that is, two blocks touching each other either orthogonally or diagonally, will never exhibit an AMR level difference exceeding one (Nool and Keppens, 2002).

The primary challenge encountered when coupling PARADISE with Icarus arose from the block-based structure of the Icarus grid when multiple levels of AMR are applied. When a particle is close to the boundary of a block, that is, when it is in some form outside the internal grid structure of the current block, communication between multiple neighbouring blocks becomes necessary to provide requisite data for numerical computation processes such as trilinear interpolation or finite volume differencing. This issue is illustrated in Fig. 4 that has been adapted from the MPI-AMRVAC documentation where further information about the AMR implementation can be found¹. In cases involving more than two levels of AMR, it becomes evident that a block of some level L must eventually communicate with either a so-called parent block of level $L - 1$, or a so-called children block of level $L + 1$. Communication between blocks of the same level occurs both with and without applied AMR.

The solution of having ghost cells for each block, as employed by the built-in particle tracer in AMRVAC, was not feasible for PARADISE due to resulting significantly larger data files storing these ghost cell values. As an alternative, we chose to individually address the various scenarios based on a particle's position relative to the numerical grid and acquire all necessary data from neighbouring blocks as needed.

3. Simulation results

In this section, we showcase simulation results obtained from the Icarus+PARADISE model. Implementing the setup described in Sec. 2.3, we first validate our new model by reproducing results of the previously established EUHFORIA+PARADISE model using in Icarus a uniform grid

¹ https://amrvac.org/md_doc_amrstructure.html

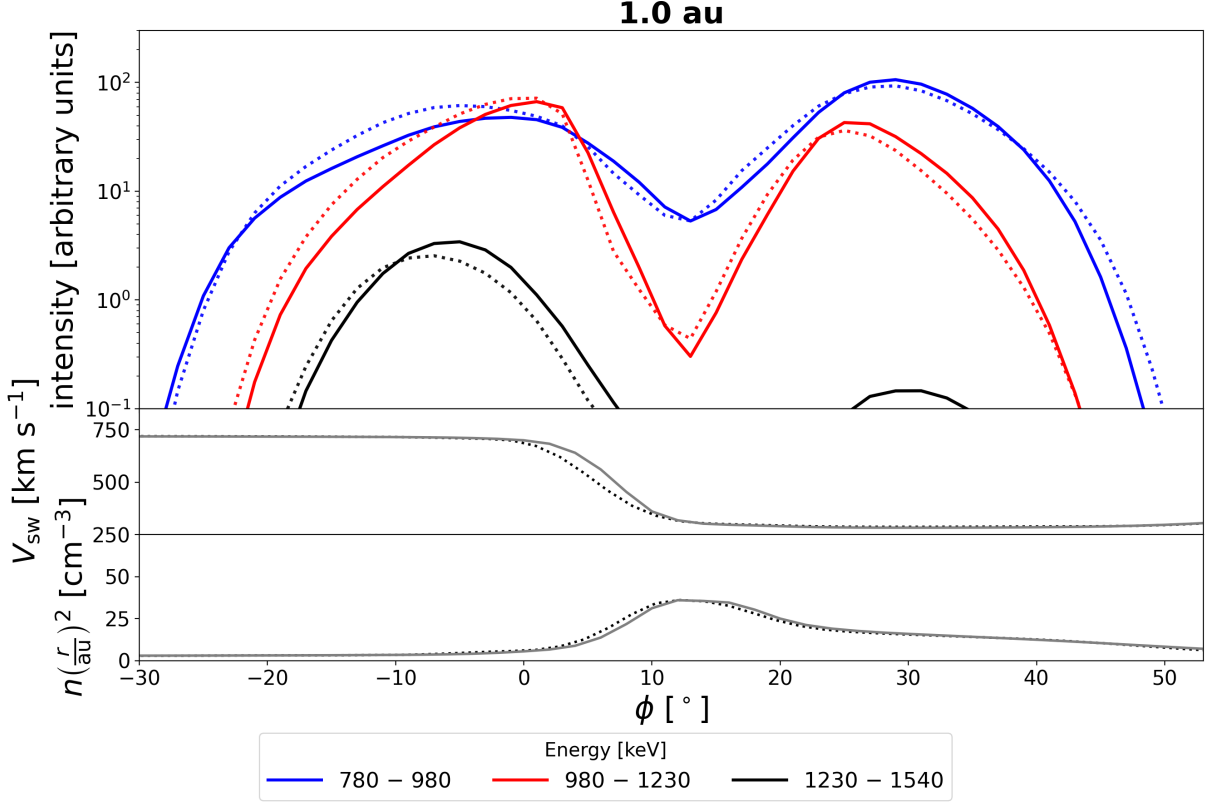


Fig. 5: Longitudinal profiles of intensities (top panel) obtained for 1 MeV protons at $\theta = 90^\circ$ and $r = 1.0$ au. The intensities obtained in the Icarus wind are represented by dotted lines, while the EUHFORIA-based trends are depicted by solid lines, each in their respective colours. Similarly, the solar wind speed and solar wind particle number density (middle and bottom panel, respectively) are shown in dotted lines for Icarus and solid lines for EUHFORIA.

(Sec. 3.1). Subsequently, we explore the impact of higher levels of AMR to illustrate its effects (Sec. 3.2).

3.1. Validation

Figures 5 and 6 show longitudinal profiles of the particle intensities obtained by PARADISE at radial distances $r = 1$ au (Fig. 5) and $r = 1.5$ au (Fig. 6). In each figure, the top panel shows the intensity profiles of three selected energy channels that are defined in the legend below the figures. Additionally, we provide the longitudinal profiles of solar wind speed (middle panel) and the particle number density (bottom panel). The Icarus-based results are shown in dotted lines, while the results obtained in the EUHFORIA wind are shown in the same figures in the same colours, but in solid lines. Similarly, the solar wind parameter profiles are shown in dotted format for Icarus and in solid for EUHFORIA.

For both models, we observe the result of adiabatic deceleration (channel below 1 MeV) and shock acceleration (channels above 1 MeV). Furthermore, the intensity profiles reveal a characteristic two-peaked structure typically associated with a CIR. The right intensity peak corresponds to

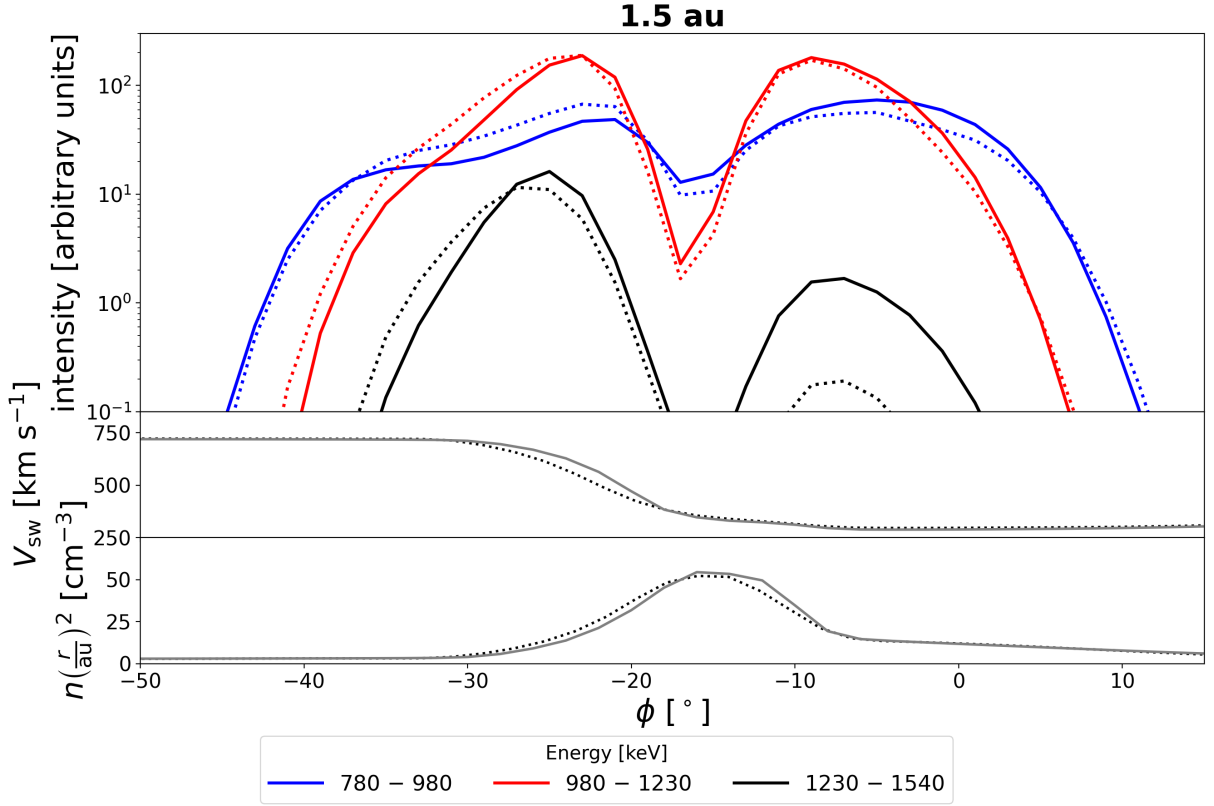


Fig. 6: Longitudinal profiles of intensities (top panel) obtained for 1 MeV protons at $\theta = 90^\circ$ and $r = 1.5$ au. The intensities obtained in the Icarus wind are represented by dotted lines, while the EUHFORIA-based trends are depicted by solid lines, each in their respective colours. Similarly, the solar wind speed and solar wind particle number density (middle and bottom panel, respectively) are shown in dotted lines for Icarus and solid lines for EUHFORIA.

particles accelerated at the forward shock of the CIR, whereas the valley between the two peaks coincides with the stream interface (SI) of the CIR, that is, the transition between the compressed slow and fast wind. The left intensity peak is attributed to particles originating from the reverse shock.

In the two lowest energy channels, the two models exhibit good agreement, resembling in shape and following a similar trend. It can be noted that, depending on the longitude, the Icarus-based intensities exceed the EUHFORIA-based results, and vice versa. These small differences can be attributed to the small differences between the underlying solar wind configurations. This variability is expected, given that the underlying models are not identical, and energetic particles traverse a significant distance through these two solar winds before reaching observers. Cumulatively, small differences in both solar winds can impact the particles' properties. Moreover, in the highest energy channel, it can be seen that the intensities in EUHFORIA peak higher than in Icarus. This difference can be attributed to the fact that, at the same resolution, Icarus exhibits a slightly higher level of diffusion compared to EUHFORIA. Consequently, the shock in Icarus is less steep than in the EUHFORIA solar wind, resulting in a reduction of particle acceleration efficiency. However, as

demonstrated in the following section, the implementation of AMR enables Icarus to achieve a resolution at the shock significantly surpassing the one depicted in Fig. 5 and 6.

3.2. Effect of AMR application

In contrast to similar heliospheric MHD models such as ENLIL or EUHFORIA, which employ uniform equidistant grids, the MPI-AMRVAC framework empowers Icarus to utilise AMR to refine regions of interest while maintaining a low resolution in other regions. We illustrate the application of five levels of AMR in the panels of Fig. 7 that are similarly structured as Figs. 5 and 6 with the longitudinal intensity profiles in the top panels, the solar wind speed profiles in the middle panels, and the solar wind particle number density in the bottom panels in each subfigure. Here, AMR level 1 corresponds to a uniform grid with the resolution as described in Sec. 2.3. The subfigures in Fig. 7 depict the intensities at $r = 1.8$ au.

Similarly to Figs. 5 and 6, we observe two peaks in the intensities, the right peak corresponding to the forward shock, and the left peak corresponding to the reverse shock. For the higher energy channels, the intensity peak associated to the forward shock becomes only visible by increasing the resolution (i.e., higher AMR level). With increasing level of AMR, the channels of higher energies, that is the channels measuring the accelerated particles, are increasingly populated. It is crucial to note that shock waves simulated by 3D MHD models are typically much wider than actual shock waves in interplanetary space. Since the ratio of the MFP length to the width of the shock plays a pivotal role, simulations with a more refined shock (here, due to higher levels of AMR) result in more efficient particle acceleration for the same MFP length, see e.g., [Wijzen et al. \(2022\)](#).

To elucidate the impact of higher levels of AMR on particle acceleration, Fig. 8 displays intensity-energy profiles at different radial distances at the reverse shock. The intensity curves consist of the peaks of the corresponding energy channel at the particular radial distance, where panel (a) show the results at 0.5 au, panel (b) at 1 au, panel (c) at 1.5 au, and panel (d) at 1.8 au. All panels consistently indicate an increase in the intensity at higher energies with increasing level of AMR.

With increasing resolution, the particle intensities and their energy spectra should converge if the underlying solar wind converges. However, it should be kept in mind that by increasing the resolution of the MHD simulation, we are resolving smaller-scaled solar wind structures, which can subsequently affect the energetic particles. While the results in Fig. 8 do not show convergence yet, the differences between consecutive AMR levels can be seen to progressively decrease.

4. Summary and discussion

The significance of energetic particles generated in the heliosphere is growing due to humanity's dependence on space technology and its renewed interest in space exploration. Consequently, there is a pressing need for the development of numerical tools to reliably and timely predict harsh events. In order to make progress in our space weather forecasting capabilities and our theoretical understanding of transport and acceleration of solar energetic particles, we have introduced the Icarus+PARADISE model. This two-part-model comprises the 3D MHD code Icarus, integrated into the MPI-AMRVAC framework, which generates solar wind background configurations. Accompanying Icarus is the energetic particle transport code PARADISE, which takes the Icarus

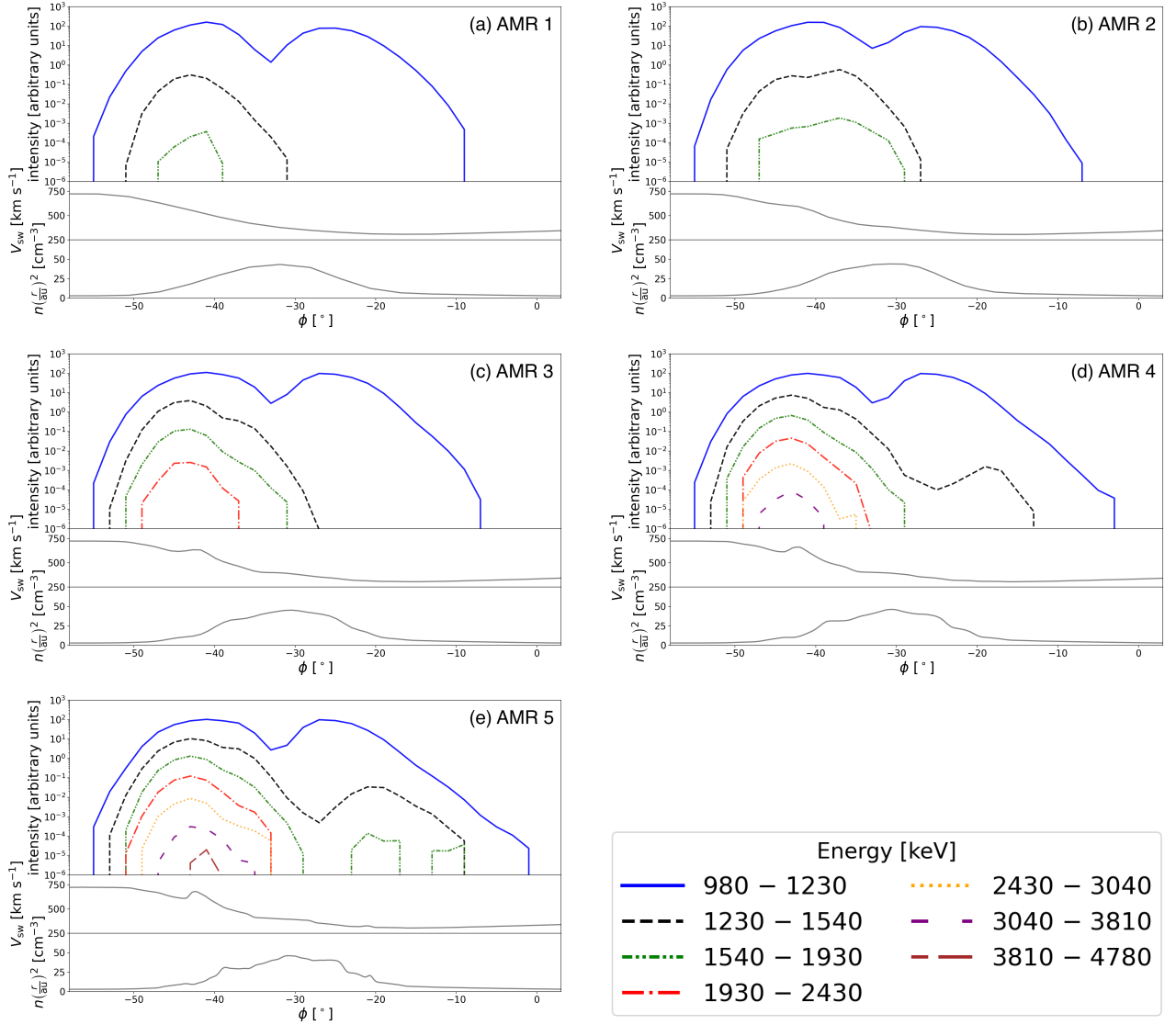


Fig. 7: Longitudinal profiles of intensities obtained for 1 MeV protons in the Icarus wind at $\theta = 90^\circ$ for five levels of AMR (panels a through e). Each plot displays intensities at $r = 1.8$ au together with the background solar wind speed (middle panels) and solar wind particle number density (bottom panels).

wind as input to propagate energetic particles as test particles through it and tracks their acceleration and deceleration by solving the FTE in a stochastic manner.

To introduce the new model, we presented a theoretical study using a synthetic solar wind map for the coronal model providing Icarus with inner boundary conditions to generate a solar wind configuration that contains two CIRs. As part of the validation process, we reproduced outcomes from the earlier EUHFORIA+PARADISE model and showcased longitudinal intensity profiles at different radial distances. The simulation results demonstrated overall good agreement, exhibiting a strong similarity in the lower energy channels. However, some disparities surfaced in the higher channels, where the intensities derived from EUHFORIA surpassed those obtained in the Icarus simulation

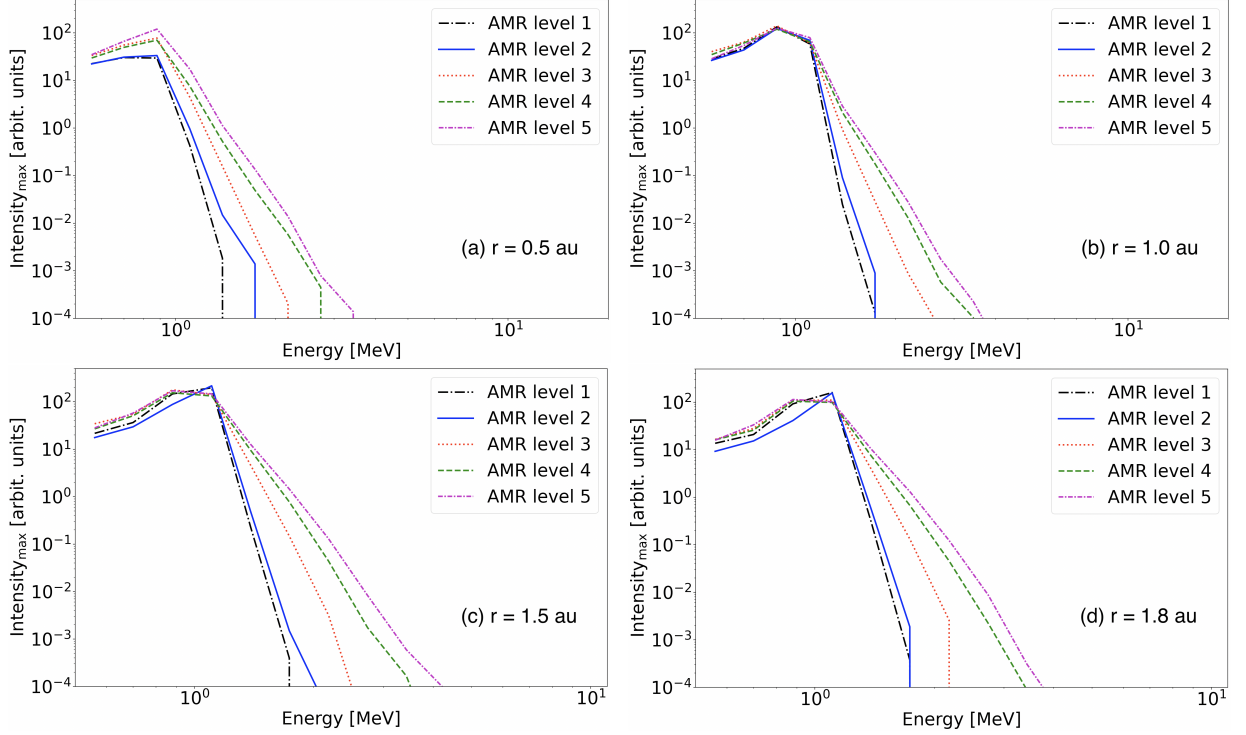


Fig. 8: Plots of intensities versus energy at $r = 0.5$ au (panel a), $r = 1.0$ au (panel b), $r = 1.5$ au (panel c), and $r = 1.8$ au (panel d), using different levels of AMR. The panels show the intensity peaks of the different energy channels at the reverse shock from a simulation up to 2 au.

for the same underlying MHD resolution. We attribute these variations in intensity profiles to differences between the two solar wind models, stemming from the distinct numerical schemes employed by EUHFORIA and Icarus. For instance, the TVDLF scheme used in Icarus for shock capturing, was found to be more diffusive compared to the one utilised in EUHFORIA. Alternative shock capturing schemes, such as the Harten-Lax-van Leer (HLL) Riemann solver or Roe-type approximate Riemann solvers, are available in the MPI-AMRVAC framework (Keppens et al., 2023) and are known to be less diffusive than the TVDLF scheme. They will be explored for evaluation in future studies due to their potential advantages.

The MPI-AMRVAC framework employed by Icarus offers the flexibility to include AMR. In our study, we strategically utilised a region criterion to refine only the shock region where we injected the test particles, while maintaining a lower resolution for the remaining solar wind. Using five levels of AMR, we displayed longitudinal profiles of the intensities at 1.8 au. Furthermore, we extracted the intensity peaks for the different energy channels and illustrated the corresponding intensity-energy plots at the reverse shock at different radial distances. Our findings consistently demonstrated that as the level of AMR increased, a more pronounced particle acceleration was observed. This result holds significant implications for models that simulate particle acceleration at shock waves generated by MHD models, see for instance, Wijzen et al. (2022) using EUHFORIA+PARADISE to study proton acceleration in the inner heliosphere, or Young et al. (2021) using EPREM and the CORona-HELiosphere (CORHEL) model to investigate proton acceleration in the corona.

In our future work, we anticipate further applications of the Icarus+PARADISE model. These potential applications encompass, among others, the examination of solar wind configurations of real events involving CMEs and observed SEP events, mirroring previous studies with EUHFORIA+PARADISE. Furthermore, Icarus is also capable to implement grid stretching, that is the ability to keep grid cells in a more cubic shape that in an otherwise equidistant grid in spherical coordinates would become more elongated. Performance of Icarus with applied radial grid stretching with combination of AMR is demonstrated in [Baratashvili et al. \(2022\)](#). Such an approach can be tested for SEP studies with sufficient AMR levels in order to gain significant speed-up in computation time, while obtaining high resolution data where needed. Furthermore, a major update for Icarus+PARADISE is foreseen, for instance, a modification of PARADISE such to load only the necessary blocks of the Icarus snapshots, rather than loading entire data files. This and other enhancements are designed to accelerate simulations inside PARADISE, enable the use of higher levels of AMR, and augment the already significant acceleration of simulation time achieved by Icarus.

Acknowledgements. The authors thank Rony Keppens and Fabio Bacchini from KU Leuven, Belgium, for fruitful discussions regarding the MPI-AMRVAC framework. In addition, the authors thank the anonymous referees for their helpful comments that improved the quality of the manuscript. E.H. is grateful to the Space Weather Awareness Training Network (SWATNet) funded by the European Union’s Horizon 2020 research and innovation program under the Marie Skłodowska-Curie grant agreement No. 955620. Furthermore, E.H. acknowledges the travel grant V477923N from the Fonds voor Wetenschappelijk Onderzoek – Vlaanderen (FWO). N.W. acknowledges support from the Research Foundation - Flanders (FWO-Vlaanderen, fellowship no. 1184319N). R.V. acknowledges the support of the Research Council of Finland (grant no. 352847). We also acknowledge support from the European Space Agency project “Heliospheric modelling techniques” (ESA Contract No. 4000133080/20/NL/CRS) as part of the GSTP (General Support Technology Programme), the projects C14/19/089 (C1 project Internal Funds KU Leuven), G.0B58.23N and G.0025.23N (WEAVE) (FWO-Vlaanderen), 4000134474 (SIDC Data Exploitation, ESA Prodex-12), and Belpo project B2/191/P1/SWiM. Computational resources and services used in this work were provided by the VSC (Flemish Supercomputer Center), funded by the Research Foundation - Flanders (FWO) and the Flemish Government – department EWI.

References

- Agueda N and Vainio R, 2013. On the parametrization of the energetic-particle pitch-angle diffusion coefficient. *J Space Weather Space Clim*, **3**, A10. <http://doi.org/10.1051/swsc/2013034>. 2.1
- Agueda N, Vainio R, Lario D and Sanahuja B, 2008. Injection and Interplanetary Transport of Near-Relativistic Electrons: Modeling the Impulsive Event on 2000 May 1. *Astrophys J*, **675**, 1601. <http://doi.org/10.1086/527527>. 2.1
- Allen RC, Ho GC, Mason GM, Li G, Jian LK et al., 2021. Radial Evolution of a CIR: Observations From a Nearly Radially Aligned Event Between Parker Solar Probe and STEREO-A. *Geophys Res Lett*, **48**, e91,376. <https://doi.org/10.1029/2020GL091376>. 1
- Bandyopadhyay R, Matthaeus WH, McComas DJ, Chhiber R, Usmanov AV et al., 2022. Sub-Alfvénic Solar Wind Observed by the Parker Solar Probe: Characterization of Turbulence, Anisotropy, Intermittency, and Switchback. *Astrophys J Lett*, **926**, L1. <https://doi.org/10.3847/2041-8213/ac4a5c>. 2.2

- Baratashvili T, Verbeke C, Wijsen N and Poedts S, 2022. Improving CME evolution and arrival predictions with AMR and grid stretching in Icarus. *Astron Astrophys*, **667**, A133. <https://doi.org/10.1051/0004-6361/202244111>. 2.2, 4
- Cane HV, Richardson IG and von Rosenvinge TT, 2010. A study of solar energetic particle events of 1997–2006: Their composition and associations. *J Geophys Res*, **115**, A08,101. <https://doi.org/10.1029/2009JA014848>. 1
- Desai M and Giacalone J, 2016. Large gradual solar energetic particle events. *Living Rev Sol Phys*, **13**, 3. <https://doi.org/10.1007/s41116-016-0002-5>. 1
- Gopalswamy N, 2018. Chapter 2 - Extreme Solar Eruptions and their Space Weather Consequences. In Buzulukova N, ed., *Extreme Events in Geospace*, 37. Elsevier. <https://doi.org/10.1016/B978-0-12-812700-1.00002-9>. 1
- Hapgood MA, 2011. Towards a scientific understanding of the risk from extreme space weather. *Adv Space Res*, **47**, 2059. <https://doi.org/10.1016/j.asr.2010.02.007>. 1
- Isenberg PA, 1997. A hemispherical model of anisotropic interstellar pickup ions. *J Geophys Res*, **102**, 4719. <https://doi.org/10.1029/96JA03671>. 2.1
- Jackel U and Schlickeiser R, 1992. Quasilinear theory of cosmic ray pitch-angle diffusion for generalized turbulence models. *Ann Geophys*, **10**, 541. 2.1
- Jian L, Russell CT, Luhmann JG and Skoug RM, 2006. Properties of Stream Interactions at One AU During 1995 – 2004. *Sol Phys*, **239**, 337. <https://doi.org/10.1007/s11207-006-0132-3>. 1
- Jiao Y, Liu YD, Ran H and Cheng W, 2024. Properties of Steady Sub-Alfvénic Solar Wind in Comparison with Super-Alfvénic Wind from Parker Solar Probe Measurements. *Astrophys J*, **960**, 42. <https://doi.org/10.3847/1538-4357/ad0dfe>. 2.2
- Jokipii JR, 1966. Cosmic-Ray Propagation. I. Charged Particles in a Random Magnetic Field. *Astrophys J*, **146**, 480. <https://doi.org/10.1086/148912>. 2.1
- Kallenrode MB, 2003. Current views on impulsive and gradual solar energetic particle events. *J Phys G Nucl Part Phys*, **29**, 965. <https://doi.org/10.1088/0954-3899/29/5/316>. 1
- Kallenrode MB, 2004. *Space Physics*. Springer Berlin, Heidelberg. <https://doi.org/10.1007/978-3-662-09959-9>. 1
- Keppens R, Meliani Z, van Marle AJ, Delmont P, Vlasis A et al., 2012. Parallel, grid-adaptive approaches for relativistic hydro and magnetohydrodynamics. *J Comput Phys*, **231**, 718. <https://doi.org/10.1016/j.jcp.2011.01.020>. 2.2
- Keppens R, Nool M, Tóth G and Goedbloed JP, 2003. Adaptive Mesh Refinement for conservative systems: multi-dimensional efficiency evaluation. *Comput Phys Commun*, **153**, 317. [https://doi.org/10.1016/S0010-4655\(03\)00139-5](https://doi.org/10.1016/S0010-4655(03)00139-5). 2.3
- Keppens R, Popescu Braileanu B, Zhou Y, Ruan W, Xia C et al., 2023. MPI-AMRVAC 3.0: Updates to an open-source simulation framework. *Astron Astrophys*, **673**, A66. <https://doi.org/10.1051/0004-6361/202245359>. 4

- Klassen A, Dresing N, Gómez-Herrero R and Heber B, 2015. First simultaneous observations of a near-relativistic electron spike event by both STEREO spacecraft. *Astron Astrophys*, **580**, A115. <https://doi.org/10.1051/0004-6361/201525700>. 2.1
- Klimas AJ and Sandri G, 1971. Foundation of the Theory of Cosmic-Ray Transport in Random Magnetic Fields. *Astrophys J*, **169**, 41. <https://doi.org/10.1086/151116>. 2.1
- Kozarev KA, Evans RM, Schwadron NA, Dayeh MA, Opher M et al., 2013. Global numerical modeling of energetic proton acceleration in a coronal mass ejection traveling through the solar corona. *Astrophys J*, **778**, 43. <https://doi.org/10.1088/0004-637X/778/1/43>. 1
- Kozarev KA, Schwadron NA, Dayeh MA, Townsend LW, Desai MI et al., 2010. Modeling the 2003 Halloween events with EMMREM: Energetic particles, radial gradients, and coupling to MHD. *Space Weather*, **8**, S00E08. <https://doi.org/10.1029/2009SW000550>. 1
- le Roux JA and Webb GM, 2009. Time-Dependent Acceleration of Interstellar Pickup Ions at the Heliospheric Termination Shock Using a Focused Transport Approach. *J Geophys Res*, **693**, 534. <https://doi.org/10.1088/0004-637X/693/1/534>. 2.1
- Luhmann JG, Mays ML, Odstrcil D, Li Y, Bain H et al., 2017. Modeling solar energetic particle events using ENLIL heliosphere simulations. *Space Weather*, **15**, 934. <https://doi.org/10.1002/2017SW001617>. 1
- Manchester IV WB, van der Holst B, Tóth G and Gombosi TI, 2012. The coupled evolution of electrons and ions in coronal mass ejection-driven shocks. *Astrophys J*, **756**, 81. <https://doi.org/10.1088/0004-637X/756/1/81>. 1
- Nool M and Keppens R, 2002. AMRVAC: a Multidimensional Grid-adaptive Magnetofluid Dynamics Code. *Comput Methods Appl Math*, **2**, 92. <https://doi.org/10.2478/cmam-2002-0005>. 2.4
- Odstrcil D, Pizzo VJ and Arge CN, 2005. Propagation of the 12 May 1997 interplanetary coronal mass ejection in evolving solar wind structures. *J Geophys Res*, **110**, A02,106. <https://doi.org/10.1029/2004JA010745>. 1
- Odstrcil D, Riley P and Zhao XP, 2004. Numerical simulation of the 12 May 1997 interplanetary CME event. *J Geophys Res*, **109**, A02,116. <https://doi.org/10.1029/2003JA010135>. 1
- Perri S, Bykov A, Fahr H, Fichtner H and Giacalone J, 2022. Recent Developments in Particle Acceleration at Shocks: Theory and Observations. *Space Sci Rev*, **218**, 26. <https://doi.org/10.1007/s11214-022-00892-5>. 1
- Petrosian V, 2016. Particle acceleration in solar flares and associated CME shocks. *Astrophys J*, **830**, 28. <https://doi.org/10.3847/0004-637X/830/1/28>. 1
- Petrosian V and Liu S, 2004. Stochastic Acceleration of Electrons and Protons. I. Acceleration by Parallel-Propagating Waves. *Astrophys J*, **610**, 550. <https://doi.org/10.1086/421486>. 1
- Pizzo VJ, 1991. The evolution of corotating stream fronts near the ecliptic plane in the inner solar system: 2. Three-dimensional tilted-dipole fronts. *J Geophys Res*, **96**, 5405. <https://doi.org/10.1029/91JA00155>. 2.3

- Pomoell J and Poedts S, 2018. EUHFORIA: European heliospheric forecasting information asset. *J Space Weather Space Clim*, **8**, A35. <https://doi.org/10.1051/swsc/2018020>. 1, 2.2, 2.3
- Reames DV, 1999. Particle acceleration at the Sun and in the heliosphere. *Space Sci Rev*, **90**, 413. <https://doi.org/10.1023/A:1005105831781>. 1
- Reames DV, 2017. Solar Energetic Particles. Springer Cham, Cham. <https://doi.org/10.1007/978-3-030-66402-2>. 1
- Richardson IG, 2004. Energetic Particles and Corotating Interaction Regions in the Solar Wind. *Space Sci Rev*, **111**, 267. <https://doi.org/10.1023/B:SPAC.0000032689.52830.3e>. 1
- Richardson IG, 2018. Solar wind stream interaction regions throughout the heliosphere. *Living Rev Sol Phys*, **15**, 1. <https://doi.org/10.1007/s41116-017-0011-z>. 1
- Roelof EC, 1969. Propagation of solar cosmic rays in the interplanetary magnetic field. In Ögelman H and Wayland J. R, eds., Lectures in High-Energy Astrophysics, 111. Scientific and Technical Information Division, Office of Technology Utilization, NASA. 2.1
- Ruffolo D, 1995. Effect of Adiabatic Deceleration on the Focused Transport of Solar Cosmic Rays. *Astrophys J*, **442**, 861. <https://doi.org/10.48550/arXiv.astro-ph/9408056>. 2.1
- Schrijver CJ, Dobbins R, Murtagh W and Petrinec SM, 2014. Assessing the impact of space weather on the electric power grid based on insurance claims for electrical equipment. *Space Weather*, **12**, 487. <https://doi.org/10.1002/2014SW001066>. 1
- Schrijver CJ, Kauristie K, Aylward AD, Denardini CM, Gibson SE et al., 2015. Understanding space weather to shield society: A global road map for 2015-2025 commissioned by COSPAR and ILWS. *Adv Space Res*, **55**, 2745. <https://doi.org/10.1016/j.asr.2015.03.023>. 1
- Skilling J, 1971. Cosmic Rays in the Galaxy: Convection or Diffusion? *Astrophys J*, **170**, 265. <https://doi.org/10.1086/151210>. 2.1
- Skilling J, 1975. Cosmic ray streaming - I. Effect of Alfvén waves on particles. *Mon Notices Royal Astron Soc*, **172**, 557. <https://doi.org/10.1093/mnras/172.3.557>. 2.1
- Smith EJ and Wolfe JH, 1976. Observations of interaction regions and corotating shocks between one and five AU: Pioneers 10 and 11. *Geophys Res Lett*, **3**, 137. <https://doi.org/10.1029/GL003i003p00137>. 1
- Strauss RD and Effenberger F, 2017. A Hitch-Hiker's Guide to Stochastic Differential Equations. *Space Sci Rev*, **212**, 151. <https://doi.org/10.1007/s11214-017-0351-y>. 2.1
- Tóth G and Odstrcil D, 1996. Comparison of some flux corrected transport and total variation diminishing numerical schemes for hydrodynamic and magnetohydrodynamic problems. *J Comput Phys*, **128**, 82. <https://doi.org/10.1006/jcph.1996.0197>. 2.3
- Vainio R and Afanasiev A, 2018. Particle Acceleration Mechanisms. In Malandraki O and Crosby N, eds., Solar Particle Radiation Storms Forecasting and Analysis, 45. Springer Cham. https://doi.org/10.1007/978-3-319-60051-2_3. 1
- van den Berg J, Strauss DT and Effenberger F, 2020. A Primer on Focused Solar Energetic Particle Transport. *Space Sci Rev*, **216**, 146. <https://doi.org/10.1007/s11214-020-00771-x>. 1

- Verbeke C, Baratashvili T and Poedts S, 2022. ICARUS, a new inner heliospheric model with a flexible grid. *Astron Astrophys*, **662**, A50. <https://doi.org/10.1051/0004-6361/202141981>. 1, 2.2, 2.3
- Wijsen N, 2020. PARADISE: A model for energetic particle transport in the solar wind. PhD dissertation, KU Leuven (Belgium) and Univ. Barcelona (Spain). 1, 2.1, 2.1, 2.1
- Wijsen N, Aran A, Pomoell J and Poedts , 2019. Modelling three-dimensional transport of solar energetic protons in a corotating interaction region generated with EUHFORIA. *Astron Astrophys*, **622**, A28. <https://doi.org/10.1051/0004-6361/201833958>. 1
- Wijsen N, Aran A, Scolini C, Lario D, Afanasiev A et al., 2022. Observation-based modelling of the energetic storm particle event of 14 July 2012. *Astron Astrophys*, **659**, A187. <https://doi.org/10.1051/0004-6361/202142698>. 2.3, 3.2, 4
- Wijsen N, Lario D, Sánchez-Cano B, Jebaraj IC, Dresing N et al., 2023. The Effect of the Ambient Solar Wind Medium on A CME-driven Shock and the Associated Gradual Solar Energetic Particle Event. *Astrophys J*, **950**, 172. <https://doi.org/10.3847/1538-4357/acd1ed>. 1
- Wijsen N, Samara E, Aran A, Lario D, Pomoell J et al., 2021. A Self-consistent Simulation of Proton Acceleration and Transport Near a High-speed Solar Wind Stream. *Astrophys J Lett*, **908**, L26. <https://doi.org/10.3847/2041-8213/abe1cb>. 1, 2.3
- Woodward P and Colella P, 1984. The numerical simulation of two-dimensional fluid flow with strong shocks. *J Comput Phys*, **54**, 115. [https://doi.org/10.1016/0021-9991\(84\)90142-6](https://doi.org/10.1016/0021-9991(84)90142-6). 2.3
- Xia C, Teunissen J, El Mallah I, Chané' E and Keppens R, 2018. MPI-AMRVAC 2.0 for Solar and Astrophysical Applications. *Astrophys J*, **234**, 30. <https://doi.org/10.3847/1538-4365/aaa6c8>. 2.2
- Young MA, Schwadron NA, Gorby M, Linker J, Caplan RM et al., 2021. Energetic Proton Propagation and Acceleration Simulated for the Bastille Day Event of 2000 July 14. *Astrophys J*, **909**, 160. <https://doi.org/10.3847/1538-4357/abdf5f>. 4